ISSN 1648-7788 / eISSN 1822-4180

VILNIUS TECH
Vilnius Gediminas Technical University

AVIATION

2026
Volume 30
Issue 2
Pages 156–170
https://doi.org/10.3846/aviation.2026.26866

BIONIC FLAPPING WING STRUCTURAL PARAMETER OPTIMIZATION BASED ON LIFT MAXIMIZATION

Haojun YANG[1], Jinglin LUO[2], Xiaoqiang LI[1], Yuguang LIANG[1], Zelin HONG[1], Jingjing ZHANG[1], Zhifeng WANG[1]

[1]*School of Mechatronic Engineering and Automation, Foshan University, Foshan, China*
[2]*Foshan Zhishi Technology Co., Ltd, Foshan, China*

Article History:
- received 22 October 2025
- accepted 16 March 2026

Abstract. To address the issues of short endurance and poor flight performance of flapping wing aircraft, this study focuses on the double-crank double-rocker two-segment flapping wing mechanism and conducts structural parameter optimization research based on lift maximization. First, the complex vector method is used to derive the kinematic models of the four-bar mechanism and the two-segment flapping wing mechanism, establishing the intrinsic relationship between "geometric parameters and flapping wing motion laws". Combined with the lift formula, a quantitative relationship between "geometric parameters, flapping velocity, and lift" is constructed. With the goal of maximizing the average lift, the genetic algorithm is applied to optimize the key geometric parameters of the mechanism. Finally, numerical simulations of the aerodynamic characteristics of the flapping wing mechanism before and after optimization are carried out to verify the optimization effect. The results show that after optimization, the swing range of the inner wing expands from approximately 57° to 90°; the folding speed of the inner and outer wings during the upstroke is significantly increased, reducing the resistance in the upstroke process; the deployment speed during the downstroke is increased, enhancing the lift in the downstroke process. Meanwhile, as the incoming flow velocity or flapping frequency increases, the growth rates of the net lift and net thrust of the optimized flapping wing are significantly higher than those before optimization. The research results of this paper provide theoretical support and technical references for the selection and parameter design of transmission mechanisms for high-performance flapping wing aircraft.

Keywords: flapping wing aircraft, bionic flapping wing, lift maximization, structural parameter optimization, aerodynamic analysis, CFD.

Corresponding author. E-mail: *jingjing@fosu.edu.cn*

1. Introduction

Unmanned aerial vehicles can generally be categorized into fixed-wing, rotary-wing, and flapping-wing configurations according to their flight principles (Zhou et al., 2022). Among these platforms, flapping-wing aircraft have attracted increasing research interest due to their potential advantages in low aerodynamic noise, enhanced maneuverability, and biological stealth characteristics inspired by natural flyers. Despite these advantages, practical applications of flapping-wing aircraft are still constrained by several key challenges, including limited flight endurance, relatively low aerodynamic efficiency, and discrepancies between artificial flapping kinematics and those observed in real birds or insects.

To improve the aerodynamic performance of flapping-wing aircraft, extensive efforts have been devoted to the optimization of flapping kinematic parameters through both numerical simulations and experimental investigations. Rakotomamonjy et al. (2007) optimized the kinematic parameters of a micro single-segment flapping wing aircraft using the genetic algorithm with the goal of maximizing the average lift. Ansari et al. (2008) investigated the effects of kinematic parameters (flapping frequency, flapping amplitude, and pitching phase) on the aerodynamic performance of insect-like flapping wings in the hovering state. Zhang et al. (2016) analyzed the aerodynamic performance of fly-like hovering flapping wings and found that the aerodynamic performance of hovering flies is mainly determined by flapping frequency and flapping amplitude. Choi et al. (2017) defined a design process for a flapping system analysis and applied to a flapping wing air vehicle model. Wang et al. (2019) systematically analyzed the effects of wingspan, flapping amplitude, flapping frequency, flapping wing stiffness, and aspect ratio on the aerodynamic performance of flapping wings. Huang (2019) optimized a double-crank-rocker flapping wing mechanism to imitate the motion of eagle wing and

verified the optimized performance by the flight tests. Bhat et al. (2020) studied the effects of different flapping and pitching motion trajectories on the aerodynamic performance of flapping wings when fruit flies hover at a fixed flapping frequency and amplitude. Gehrke and Mulleners (2020) optimized the pitch angle trajectory of hovering flapping wings using a model test method and concluded that a trapezoidal pitch angle trajectory has better aerodynamic performance. Zheng et al. (2020) found through the analysis of the kinematic parameters of ellipsoidal 3D flapping wings that a sinusoidal flapping trajectory with high flapping amplitude and medium pitching amplitude can significantly increase the lift coefficient of the flapping wings. Addo-Akoto et al. (2021) segmented the flapping wing motion trajectory and used numerical calculation methods to study the effects of flapping motion duration and pitching motion phase changes on the aerodynamic performance of flexible and rigid hovering flapping wings. Lang et al. (2021) numerically studied the aerodynamic characteristics of owl-like flapping wings under two different flapping-pitching motion trajectories. Liu et al. (2022) studied and optimized the flight speed, angle of attack, flapping amplitude, and flapping frequency of beetle-like forward-flying flapping wings through wind tunnel tests. Zhang et al. (2022) analyzed the aerodynamic characteristics of butterfly-like flapping wings using numerical calculations and investigated the effects of changes in flapping amplitude, flapping-pitching phase difference, pitch angle, and incoming flow velocity on the aerodynamic forces generated by the flapping wings. Dong et al. (2023) took a hummingbird-inspired reversible hovering flapping wing as the research object, obtained a high-efficiency flapping wing design meeting the requirements through surrogate optimization, and conducted a sensitivity analysis on the optimized parameters to reveal the design rules of hummingbird-bionic flapping wings. Xu et al. (2024) analyzed the influences of three kinematic parameters, such as reduced frequency, flapping amplitude and pitching amplitude, on the aerodynamic performance of flapping wing by the combination of the Taguchi test and numerical solution of three-dimensional N-S equation, to improve the lifting efficiency of the flapping wing. Ling et al. (2025) performed multi-objective optimization on parameters such as link length, flapping amplitude, and transmission angle amplitude with the goals of minimizing flight energy consumption and motor peak torque. Li et al. (2025) derived the kinematic and energy equations of the flapping wing mechanism theoretically with the goal of minimizing the maximum transmission angle during the flapping wing motion and optimized the flapping wing mechanism using the NAGA-II algorithm to improve the mechanism stability. These studies indicate that appropriate kinematic optimization can significantly enhance aerodynamic performance under hovering and forward-flight conditions.

The flapping velocity of flapping wing aircraft is one of the key factors restricting their mechanical performance, and the motion parameter laws of flapping wings directly determine their flapping velocity. The structure of single-segment flapping wing aircraft is relatively simple, and the flapping wing motion laws can be directly controlled by servos. Therefore, most of the above studies take the single-rotor flapping wing mechanism as the analysis object through numerical simulation or experimental methods to optimize the motion parameters of the flapping wing mechanism. Multi-segment flapping wing structures have higher aerodynamic performance than single-segment ones. Taking the two-segment flapping wing structure as an example, to improve the phase synchronization and amplitude consistency of the inner and outer wings, this study takes the double-crank double-rocker two-segment flapping wing mechanism as the research object to optimize its aerodynamic performance. Geometric parameters are the main factors affecting the motion laws of this flapping wing mechanism. Starting from the basic theory of lift, this paper explores the intrinsic relationship between "geometric parameters - motion laws - flapping velocity - flapping wing aerodynamic performance", derives the kinematic model of the double-crank double-rocker two-segment flapping wing mechanism theoretically, and establishes a quantitative relationship between "geometric parameters - flapping velocity - lift". Then, with the maximization of average lift as the optimization goal, the optimization design of the key geometric parameters of the mechanism is carried out. Finally, the flapping velocity characteristics and aerodynamic performance before and after optimization are compared through numerical simulations, providing technical references for the selection and parameter design of transmission mechanisms for high-performance flapping wing aircraft.

Unlike most existing studies that focus on single-segment flapping wings or the optimization of kinematic parameters such as flapping amplitude and frequency, this study investigates the geometric parameter optimization of a double-crank double-rocker two-segment flapping wing mechanism. The coupling motion between the inner and outer wings introduces higher kinematic complexity, making geometric parameter optimization more challenging than that of single-segment mechanisms. By establishing a quantitative relationship between geometric parameters, flapping velocity, and aerodynamic lift, this work provides a design-oriented optimization framework that directly links transmission mechanism geometry to aerodynamic performance. The proposed approach offers new insights into the structural design of high-performance multi-segment flapping wing aircraft and complements existing kinematic optimization studies.

2. Kinematic model of the double-crank double-rocker two-segment flapping wing mechanism

As shown in Figure 1, this study takes a typical double-crank double-rocker flapping wing mechanism as the

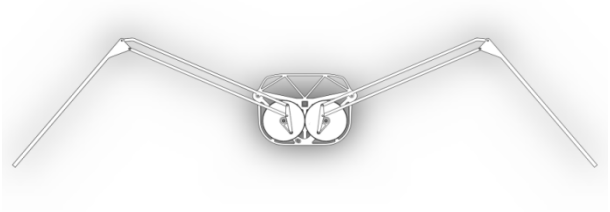

Figure 1. Schematic diagram of a two-segment flapping wing aircraft mechanism driven by a crank-rocker mechanism

research object. One side of the mechanism consists of two four-bar mechanisms: the up-down flapping of the inner wing is realized by the inner crank-rocker mechanism, and the folding and deployment of the outer wing are realized by the outer double-rocker mechanism.

2.1. Kinematic analysis of the four-bar mechanism

The flapping wing mechanism is composed of two sets of four-bar mechanisms. This paper first of all conducts a kinematic analysis of this mechanism. As shown in Figure 2, in the four-bar mechanism, OA is the driving link, AB is the connecting link, BC is the follower link, and OC is the frame. The mechanism takes O as the origin, defines the direction of the frame as the x-axis, and the vertical direction as the y-axis. is the angle between OA and the horizontal direction, $\Phi 2$ is the angle between AB and the horizontal direction, and $\Phi 3$ is the angle between BC and the horizontal direction.

The complex vector method is used to establish the kinematic model of the four-bar mechanism:

$$\overrightarrow{OA}+\overrightarrow{AB}=\overrightarrow{CB}+\overrightarrow{OC}; \tag{1}$$

$$\begin{aligned} l_{OA}\sin\varphi_1+l_{AB}\sin\varphi_2&=l_{CB}\sin\varphi_3\\ l_{OA}\cos\varphi_1+l_{AB}\cos\varphi_2&=l_{CB}\cos\varphi_3+l_{OC}\end{aligned}. \tag{2}$$

After organizing the above formulas, we can obtain:

$$\begin{aligned} &A\cos\varphi_3+B\sin\varphi_3+C=0\\ &A=l_{OC}-l_{OA}\cos\varphi_1\\ &B=-l_{OA}\sin\varphi_1\\ &C=\frac{A^2+B^2+l_{CB}^2-l_{AB}^2}{2l_{CB}}\end{aligned}. \tag{3}$$

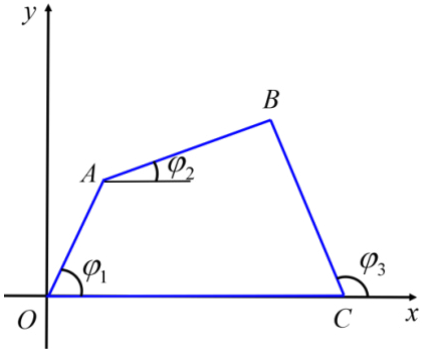

Figure 2. Schematic diagram of the four-bar mechanism

2.2. Kinematic model of the double-crank double-rocker two-segment flapping-wing mechanism

Based on the kinematic derivation of the four-bar mechanism, this section analyzes the kinematic model of the double-crank double-rocker two-segment flapping wing mechanism. As shown in Figure 3, CC_1 is the inner wing part, which flaps up and down around point C. OA, AB, BC, and CO are the four connecting rods for motion control of the inner wing mechanism. C_1D is the outer wing part; the link C_1D and the link B_1C_1 form a fixed angle, and the link C_1D moves with the link B_1C_1. Therefore, O_1A_1, O_1C_1, B_1C_1, and A_1B_1 are the four connecting rods for motion control of the outer wing mechanism.

As shown in Figure 3, this flapping wing mechanism realizes the up-down flapping and folding of the inner and outer wings through the coordinated motion of the blue four-bar mechanism OABC and the red four-bar mechanism $O_1A_1B_1C_1$. Local coordinate systems are established for the two four-bar mechanisms respectively for analysis. The angle between the local coordinate system and the body (global) coordinate system is θ_0. In the subsequent analysis, parameters with the subscript "*in*" represent the inner wing mechanism, and those with the subscript "*out*" represent the outer wing mechanism.

The frame OC of the inner wing driving mechanism is fixed on the aircraft body. The driving link OA is driven by a motor to rotate around point O. OA transmits the rotation of the motor to the follower link BC through the connecting link AB, making it swing around point C and driving the inner wing CC_1 to flap up and down around point C. The angle between the inner wing and the y-axis of the body coordinate system is denoted as θ_1, and its expression is:

$$\theta_1=\frac{3\pi}{2}-\beta_1-\varphi_{3-in}. \tag{4}$$

The driving link O_1A_1 of the outer wing mechanism is in a fixed constraint with the connecting link AB of the inner wing mechanism, and the angle between them is β_3. The link O_1A_1 rotates with the connecting link AB of the inner

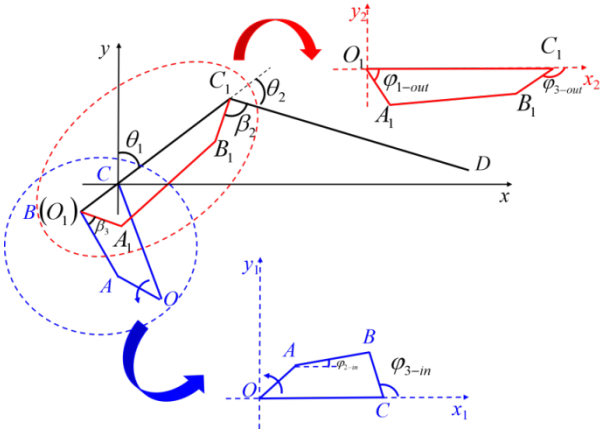

Figure 3. Schematic diagram of the four-bar mechanism

wing. The rotation angle of the driving link O_1A_1 and the frame O_1C_1 in the outer wing mechanism is denoted as φ_1-out, and its expression is:

$$\varphi_{1-out} = \varphi_{3-in} - \varphi_{2-in} - \beta . \tag{5}$$

The driving link O_1A_1 transmits motion to the follower link B_1C_1 through the connecting link A_1B_1. The link C_1D and the link B_1C_1 form a fixed angle, and the link C_1D moves with the link B_1C_1. Therefore, the swing angle θ_2 of the outer wing relative to the inner wing is expressed as:

$$\theta_2 = \varphi_{3-out} - \beta_2 . \tag{6}$$

Combining Equations (3) to (6), the relational expressions between θ_1, θ_2 and the geometric parameters of the flapping wing mechanism can be derived, establishing the intrinsic relationship between "geometric parameters and flapping wing motion laws" of the flapping wing mechanism.

3. Optimization of key geometric parameters of the flapping wing mechanism

3.1. Objective function

The lift experienced by an object during motion is expressed as:

$$L = \frac{1}{2}\rho S C_L V_S^2 , \tag{7}$$

ρ is the air density of the environment where the object is located, V_S is the relative velocity between the object and the air, S is the surface area of the object, and C_L is the lift coefficient of the object.

It can be seen from Equation (7) that assuming C_L is constant during the flapping wing motion, the key to the lift magnitude lies in the relative velocity V_S between the wing and the air. The magnitude of V_S is affected by the incoming flow velocity and the flapping velocity of the flapping wing. As shown in Figure 4, the upper part of the figure shows the airfoil section of the flapping wing, and the horizontal incoming flow velocity is V_∞. When the flapping wing moves downward, the linear velocity of the airfoil section is denoted as V_f (direction: vertically downward), and the air velocity relative to the wing surface is denoted as V_R (with the same magnitude as V_f, but opposite direction). The relative velocity between the wing surface and the air is the resultant velocity of V_R and V_∞, with a direction forming an angle φ with the incoming flow direction. For the convenience of analysis, the wing surface is rotated clockwise by φ; at this time, the relative velocity between the wing surface and the air is in the horizontal direction, the angle of attack of the wing surface is φ, and both V_S and φ change with time:

$$\varphi = \arcsin\frac{V_R}{V_S} . \tag{8}$$

As shown in Figure 5, take any point P on the inner wing segment CC_1; the distance from point P to the origin C is denoted as l_{CP}. Take any point Q on the outer wing C_1D; the distance from point Q to point C_1 is denoted as l_{C_1Q}. The length ratio of the inner wing CC_1 to the outer wing C_1D is 1:l.

As shown in Figure 3, θ_1 and θ_2 are the angles between the inner wing and the y-axis, and between the outer wing and the extension of the inner wingspan, respectively. The rate of change of these angles determines the flapping velocity of the flapping wing, which in turn affects the lift magnitude of the flapping wing. The rotational angular velocity of the inner wing CC_1 and the rotational angular velocity of the outer wing C_1D relative to the inner wing are respectively:

$$\omega_{in} = \dot{\theta}_1 \quad \omega_{out-in} = \dot{\theta}_2 . \tag{9}$$

The linear velocity of any point P on the inner wing CC_1 is:

$$v_P = l_{CP}\dot{\theta}_1 . \tag{10}$$

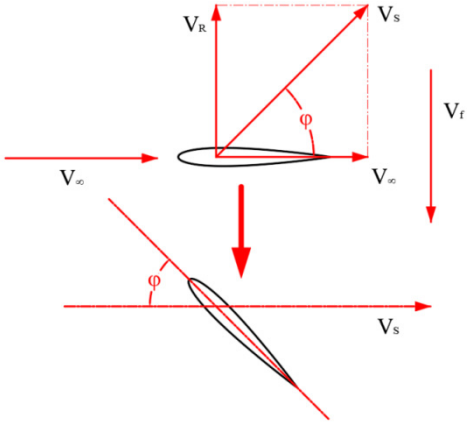

Figure 4. Schematic diagram of the four-bar mechanism

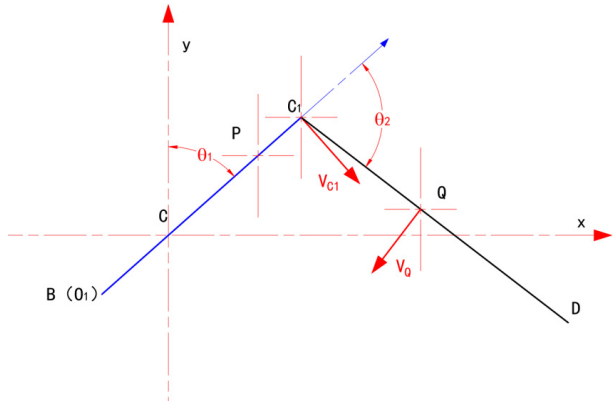

Figure 5. Schematic diagram of the four-bar mechanism

The linear velocity of point C_1 is:

$$v_{C_1} = \dot{\theta}_1. \tag{11}$$

The linear velocity of any point Q on the outer wing C_1D is:

$$v_Q = v_{C_1} + l_{C_1Q}\dot{\theta}_2. \tag{12}$$

Assuming the air density is uniform everywhere, the magnitude of L in Equation (7) is mainly related to the linear motion velocity of the flapping wing. As shown in Figure 5, at the same time, the magnitudes of the air forces on the inner wing CC_1 and the outer wing C_1D in the vertical direction during the flapping motion are:

$$L = -\frac{1}{2}\rho S C_L \int \left(\int_0^1 \operatorname{sgn}(v_{P_V}) \left(\frac{v_{P_V}}{\sin\left(\arctan\frac{v_{P_V}}{v_\infty}\right)} \right)^2 ds + \int_1^{1+l} \operatorname{sgn}(v_{Q_V}) \left(\frac{v_{Q_V}}{\sin\left(\arctan\frac{v_{Q_V}}{v_\infty}\right)} \right)^2 ds \right) dt$$

$$v_{P_V} = v_P \sin\theta_1 = s\dot{\theta}_1 \sin\theta_1$$

$$v_{Q_V} = \dot{\theta}_1 \sin\theta_1 + s\dot{\theta}_2 \sin(\theta_1 + \theta_2). \tag{13}$$

Equation (13) provides a theoretical estimation of lift variation based on flapping kinematics and relative velocity, serving as a design-oriented objective function rather than an exact aerodynamic model. When the flapping wing moves downward, the air exerts an upward force on the flapping wing; therefore, a negative sign is introduced in Equation (13) to indicate the direction relationship. Thus, the quantitative relationship between "flapping wing motion laws - flapping velocity - lift" is established. Combined with the intrinsic relationship between "geometric parameters - flapping wing motion laws" of the flapping wing mechanism, the quantitative relationship between "flapping wing geometric parameters - lift" is finally established. Combined with Equations (3–6) and Equation (13), L is determined as the objective function.

3.2. Optimization and analysis of geometric parameters of the flapping wing mechanism

With the maximization of L as the objective function, the genetic algorithm is used to optimize the geometric parameters of the four-bar mechanism in Section 2.1. The genetic algorithm parameters are summarized in Table 1. The population size and iteration number were selected based on convergence stability and computational cost. The objective function converges after approximately 96 generations, which is shown in Figure 6, indicating the robustness of the optimization process. The geometric parameters were constrained to ensure continuous rotation of the crank, avoid link interference, and satisfy structural size limitations. The parameters before and after optimization are shown in Table 2.

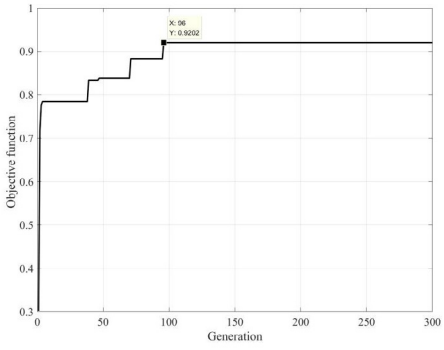

Figure 6. Schematic diagram of the four-bar mechanism

Table 1. Parameters of genetic algorithm

Parameter	Value
Population Size	200
Max Generations	300
Crossover probability	0.8
Mutation probability	0.1
Selection method	Tournament
Elitism	Enabled (top 2 individuals)
Parameter	200

Table 2. Parameters of the two-segment flapping wing driving mechanism before and after optimization

Type	Range	Before Optimization	After Optimization
Follower link CB of the inner wing driving mechanism	0.1–0.3	0.21	0.21
Frame OC of the inner wing driving mechanism	0.5–1.5	1.18	1.43
Driving link OA of the inner wing driving mechanism	0.3–0.7	0.47	0.70
Connecting link AB of the inner wing driving mechanism	0.5–1.5	0.91	1.17
Driving link O_1A_1 of the outer wing driving mechanism	0.05–0.2	0.076	0.06
Connecting link A_1B_1 of the outer wing driving mechanism	0.8–2	1.17	1.2
Follower link C_1B_1 of the outer wing driving mechanism	0.05–0.2	0.072	0.06
Frame O_1C_1 of the outer wing driving mechanism	0.8–2	1.21	1.21
β_1	0-pi	45°	90°
β_2	0-pi/2	80°	20°
β_3	0-pi/3	10°	9°

Assuming the rotational angular velocity of the crank OA is (2π×5) rad/s, the curves of θ_1 and θ_2 changing with time before and after optimization are shown in Figure 7, and the upper flapping limit and lower flapping limit positions are shown in Figure 8.

It can be seen from Figures 7 and 8 that before optimization, when the inner wing moves to the lowest point, θ_1 = 123.046°; when it moves to the highest point, θ_1 = 66.305°, with a swing range of approximately 57°. At the upper limit position, the angle between the inner and outer wings is approximately 112°. After optimization, when the inner wing moves to the lowest point, θ_1 = 98.968°; when it moves to the highest point, θ_1 = 9.119°, with a swing range of approximately 90°. At the upper limit position, the angle between the inner and outer wings is approximately 21°. Compared with the flapping wing mechanism before optimization, the optimized flapping wing mechanism has a faster folding speed of the inner and outer wings during the upstroke within the same time, a smaller angle between them after folding, and a smaller projected area of the folded wing surface, which can effectively reduce the resistance during the upstroke.

The rotational angular velocities of the inner and outer wings of the flapping wing before and after optimization are calculated based on θ_1 and θ_2 shown in Figure 7, as shown in Figure 9. The results show that during the upstroke of the flapping wing mechanism, the maximum angular velocity of the outer wing relative to the inner wing is approximately 19 rad/s before optimization and approximately 80 rad/s after optimization. Before optimization, the maximum angular velocity of the inner wing during the upstroke is approximately 15 rad/s, and that during the downstroke is approximately 21 rad/s. After optimization, the maximum angular velocity of the inner wing during

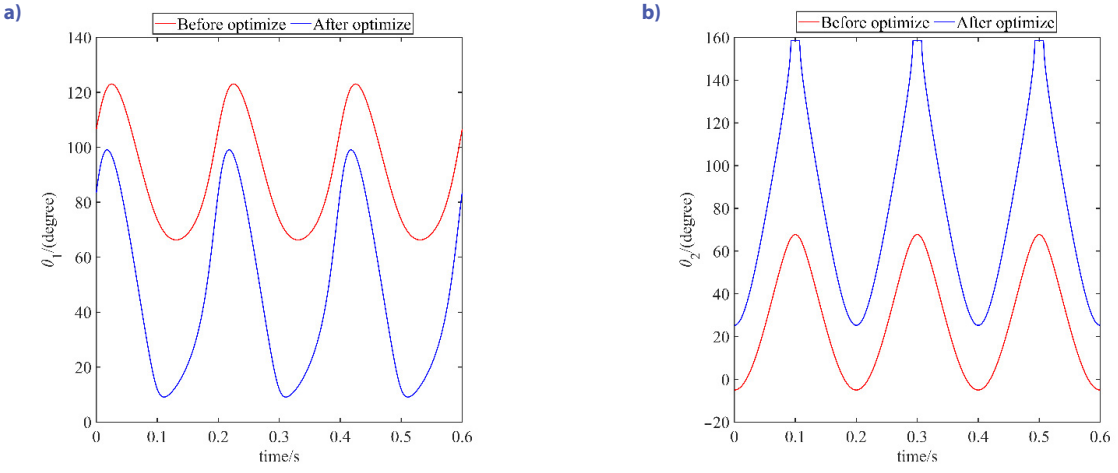

Figure 7. Curves of θ_1 and θ_2 changing with time before and after optimization: (a) – motion attitude of θ_1; (b) – motion attitude of θ_2

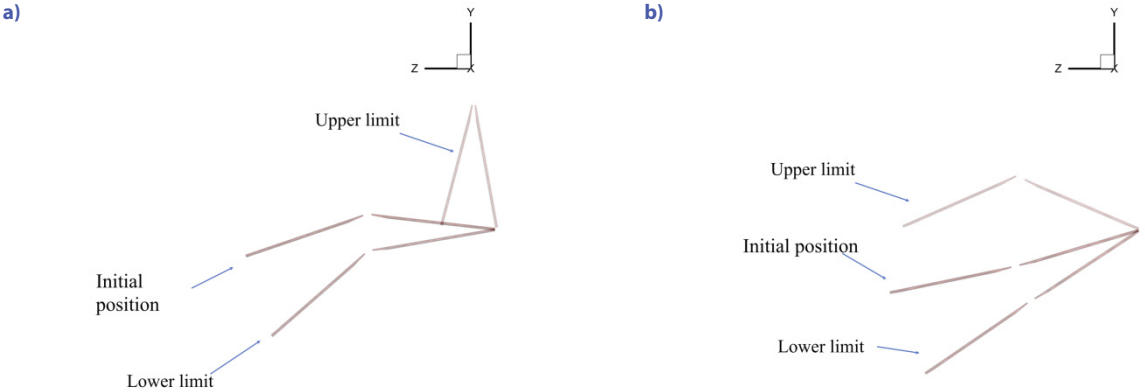

Figure 8. Motion attitudes of the flapping wing mechanism before and after optimization (a) – motion attitude of flapping wing mechanism before optimization; (b) – motion attitude of flapping wing mechanism after optimization

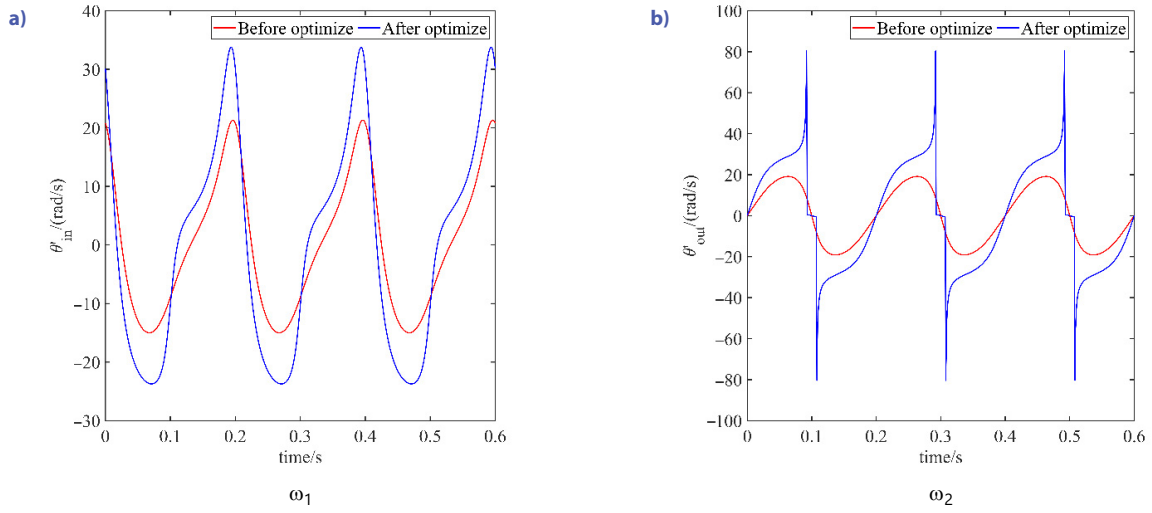

Figure 9. Curves of rotational angular velocities of the inner and outer wings of the flapping wing before and after optimization: (a) – curves of ω_1; (b) – curves of ω_2

the upstroke is approximately 24 rad/s, and that during the downstroke is approximately 34 rad/s.

The results in Figure 9 show that during the upstroke, compared with the flapping wing mechanism before optimization, the optimized one has a higher folding rate of the inner and outer wings and a smaller angle between them after folding. With the decrease of the angle, the horizontal projected area of the wing surface during the upstroke is reduced, which can effectively reduce the air resistance on the flapping wing during the upstroke. During the downstroke, the optimized wing has a higher deployment rate of the inner and outer wings, which increases the lift on the flapping wing during the downstroke.

4. Aerodynamic characteristic analysis of the flapping wing mechanism

To evaluate the aerodynamic performance of the flapping-wing mechanism, three-dimensional unsteady numerical simulations are carried out. The motion laws of the inner and outer wings of the flapping wing mechanism before and after optimization are calculated according to Equations (4) and (6), and a UDF program is compiled. Fluent is used to simulate the aerodynamic performance of the flapping wing mechanism before and after optimization. As shown in Figure 10, NACA0012 airfoil was selected for the flapping wing in this study. As a symmetric airfoil, NACA0012 does not introduce inherent lift bias under zero mean angle of attack, allowing the aerodynamic forces to be primarily governed by flapping kinematics and unsteady flow mechanisms rather than airfoil camber effects. This choice helps isolate the influence of geometric parameter optimization on aerodynamic performance. Moreover, NACA0012 has been widely adopted as a baseline airfoil in previous numerical and experimental studies on flapping wing aerodynamics, facilitating comparison with existing literature. Its moderate thickness also provides a reasonable balance between structural feasibility and numerical stability in dynamic mesh simulations. The lengths of the inner and outer wingspans on one side are both 300 mm. The fluid domain has a size of 1800 mm × 1200 mm × 1200 mm. Accordingly, the computational domain was defined with an upstream distance of 10c, a downstream distance of 20c, ±10c in the vertical direction, and 10c in the spanwise direction. This domain size is consistent with commonly adopted configurations in unsteady flapping-wing aerodynamic simulations and is sufficient to minimize boundary interference effects. The upstream boundary ensures a stable development of the incoming flow, while the extended downstream region allows the primary wake structures and vortex shedding to evolve without significant reflection from the outlet boundary. In addition, the lateral and spanwise boundaries are placed sufficiently far from the wing to reduce confinement effects. Since the primary objective of this study is a comparative evaluation of aerodynamic performance before and after geometric optimization under identical numerical conditions, the

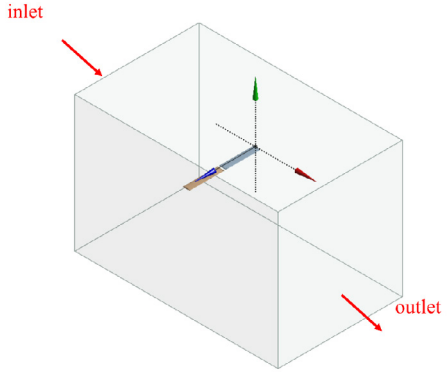

Figure 10. Aerodynamic model of the flapping wing

selected computational domain is considered adequate for capturing the relative differences in lift and thrust characteristics.

A grid independence study is conducted to assess the influence of mesh resolution. Table 3 shows the grid information parameters and post-simulation results for grid independence verification.

Since the lift curve and drag curve cannot intuitively reflect the effective lift and effective thrust obtained by the flapping wing in two cycles, this paper uses the lift impulse and drag impulse of the flapping wing to reflect the lift performance of the flapping wing before and after optimization. These two impulses represent the momentum changes of the flapping wing in the lift direction and drag direction, respectively, and their Equations are:

$$I_L = \int_0^{2T} L dt \; ; \tag{14}$$

$$I_D = \int_0^{2T} D dt \; , \tag{15}$$

where L and D are the lift and drag of the flapping wing, respectively. When the net drag impulse is negative, it represents net thrust.

Table 3 shows that the calculated results of lift impulse and drag impulse for the second and third groups are close to each other. The number of grid cells in the third group is approximately twice that in the second group, while the difference in calculation accuracy is negligible: the lift impulse error is about 0.32% and the drag impulse error is about 6.25%. However, the computation time of the third group is nearly twice that of the second group. To ensure calculation accuracy while improving computational efficiency, the grid parameters of the second group were adopted for all subsequent simulations.

4.1. Aerodynamic characteristic analysis of the flapping wing before and after optimization

Although the flapping frequency remains the same before and after optimization, the wingtip velocity increases due to geometric changes, resulting in different effective Reynolds numbers. This study focuses on the comparative aerodynamic performance induced by structural parameter optimization under identical actuation conditions, rather than strict Reynolds number similarity.

Taking the working condition with a flapping frequency f = 5 hz and an incoming flow velocity V_∞ = 1 m/s as an example, the aerodynamic characteristics of the flapping wing before and after optimization are analyzed. Figure 11 shows the comparison diagrams of the lift, rotational angular velocity of the inner wing, and rotational angular velocity of the outer wing of the flapping wing mechanism before and after optimization, where the red curve represents the flapping wing before optimization and the blue curve represents the optimized one.

Figure 12 shows that the lift of the optimized flapping wing is significantly improved. Before optimization, the lift impulse of the flapping wing is I_L = 0.0795 $N \times s$, and the thrust impulse is $I_T = -I_D$ = 0.0059 $N \times s$. After optimization,

Table 3. Grid information parameters and post-simulation results for grid independence verification

Paramete/group	1	2	3
The number of grid node	992774	3453079	6304418
The number of grid cell	725920	2541725	4652282
Run time	1 h 53 min.	7 h 22 min.	12 h 53 min.
Lift impulse	0.0584	0.0618	0.0616
Drag impulse	–0.0104	–0.0135	–0.0144

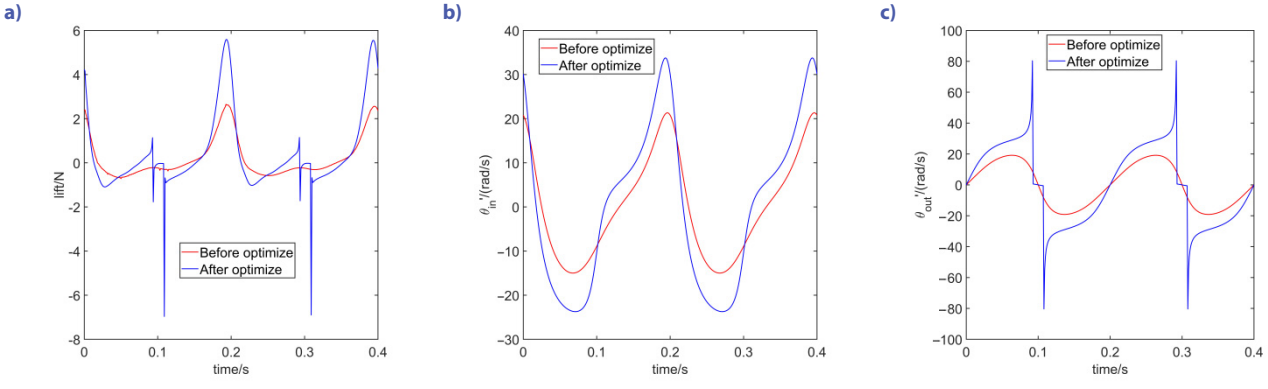

Lift Curve

Inner Wing Rotational Angular Velocity Curve

Outer Wing Rotational Angular Velocity Curve

Figure 11. Comparison diagrams of lift, rotational angular velocities of the inner and outer wings of the flapping wing before and after optimization (f = 5 hz, V_∞ = 1 m/s)

the lift impulse of the flapping wing is I_L = 0.1596 $N \times s$, and the thrust impulse is I_T = 0.0278 $N \times s$. It can be seen that the lift impulse is increased by 100.75%, and the thrust impulse is increased by 371.2%.

Taking the cross-section at three-quarters of the inner wingspan and the cross-section at three-quarters of the outer wingspan as the analysis objects, the vorticity distribution law of the flapping wing structure at the cross-section positions before and after optimization is studied. Figure 12 shows the vorticity distribution diagrams of the flapping wing cross-sections at different positions before and after optimization.

From the perspective of the vorticity distribution law, during the cyclic motion of the flapping wing (downstroke - upstroke - downstroke), the vorticity distribution of the inner and outer wing cross-sections after optimization shows better dynamic evolution characteristics: in the initial stage of the downstroke, both the inner and outer wings form concentrated and high-intensity vortex structures; during the downstroke to the lower limit, the vortex structures expand but the core intensity remains high; the peak vorticity intensity of the inner and outer wings after optimization is increased by approximately 13%, and the vorticity decay rate during the upstroke is slow with a clear structural shape. Compared with the leading-edge vortex before optimization, the attachment time of the optimized leading-edge vortex is extended by at least 50%, reflecting the cyclic stability of the vortex structure. In addition, the spatial distribution of the vortex structures of the inner and outer wings is improved: before optimization, the vorticity distribution of the inner wing is dispersed, the area of the high-vorticity region is small, the vortex structure of the outer wing is chaotic, the development of the vortices of the inner and outer wings is not synchronized, the vorticity dissipates quickly, and the flow separation is serious. After optimization, the area of the high-vorticity region of the inner wing is expanded by approximately 30%, the vortex structures of the inner and outer wings develop coordinately, the vorticity develops orderly backward, and a coherent vortex street is formed. Based on the above analysis, the lift of the flapping wing mechanism is improved because the optimized leading-edge vortex has higher intensity and longer attachment time; judging from the wake vortex structure, the wake vortex structure before optimization is unclear and the thrust generation efficiency is low, while the optimized one forms a relatively orderly reverse Kármán vortex street, and the thrust generation efficiency is significantly improved, which is consistent with the calculation results of the lift impulse and thrust impulse. This conclusion indicates that the optimized flapping wing mechanism effectively improves the aerodynamic lift of the wing, reduces energy loss, and enhances aerodynamic efficiency.

4.2. Effect of different incoming flow velocities on the aerodynamic characteristics of the flapping wing

During the actual flight of the flapping wing, it is affected by complex factors in the surrounding environment, among which the incoming flow velocity has the most direct and obvious impact on its flight. To understand the effect of incoming flow velocity on its aerodynamic characteristics, under the working condition with a flapping frequency of 5 Hz, the incoming flow velocities are set to 1 m/s, 3 m/s, and 5 m/s respectively. Figure 13 shows the effect of incoming flow velocity on the lift and thrust of the flapping wing, and Table 4 shows the lift impulse and net thrust impulse of the flapping wing structure under different working conditions.

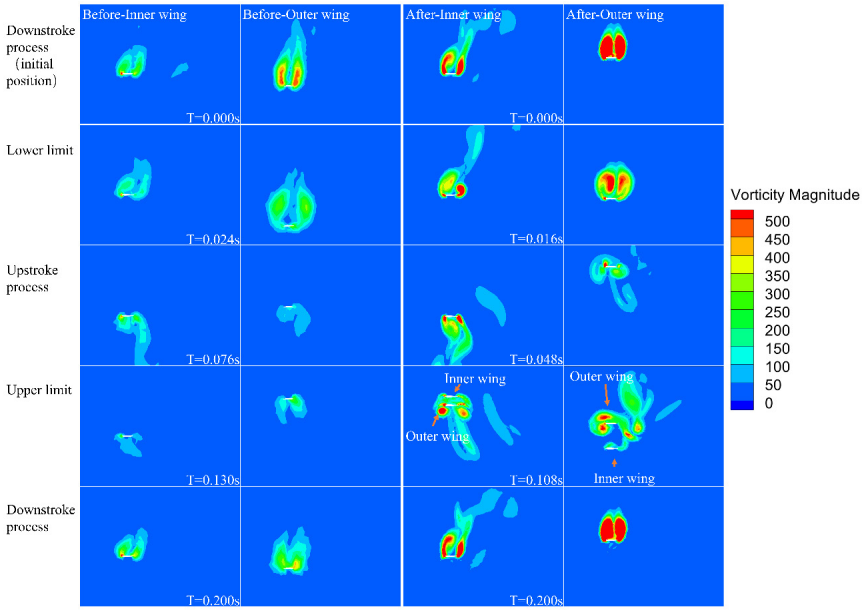

Figure 12. Vorticity distribution diagrams of the flapping wing cross-sections at different stages before and after optimization (f = 5 hz, V_∞ = 1 m/s)

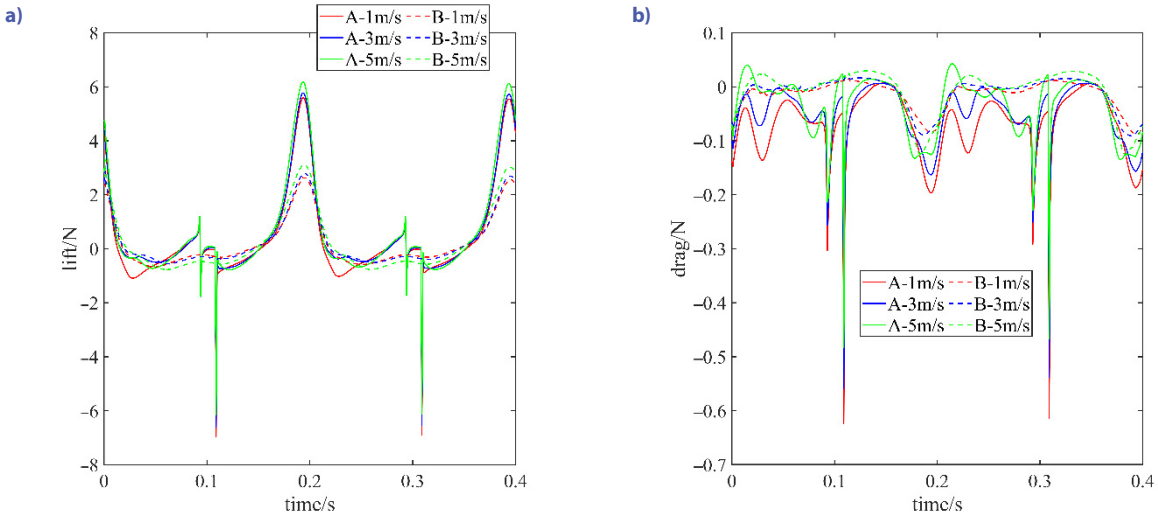

Figure 13. Lift curve and drag curve of the flapping wing under different incoming flow velocities (f = 5 hz): (a) – lift curve; (b) – drag curve

It can be found from Figure 13 that the lift and drag curves of the optimized flapping wing have discontinuities. Combined with the angle change curves of the inner and outer wings in Figure 7 and the rotational angular velocity curves of the inner and outer wings in Figure 9, the inner and outer wings of the flapping wing structure fold quickly at the discontinuities of the lift and drag curves, with a large folding angle, resulting in force discontinuities. It can be seen from Figure 13 and Table 4 that under a certain flapping frequency, as the incoming flow velocity increases, the net lift on the flapping wing increases. At the same time, the net lift and its growth rate, net thrust and its growth rate generated by the optimized flapping wing model are much higher than those before optimization.

Figures 14 and 15 show the vorticity distribution diagrams of the flapping wing cross-sections before and after optimization under the incoming flow velocity conditions of 3 m/s and 5 m/s, respectively.

It can be seen from Figures 12, 14, and 15 that under the same flapping frequency and different incoming flow velocities, the optimized flapping wing structure still exhibits concentrated and compact vortex cores, the area of the high-vorticity region is expanded by approximately 30%, the attachment time of the leading-edge vortex is extended, and the aerodynamic performance is still better. Even when the incoming flow velocity reaches 5 m/s, the key regions such as the inner and outer wings can still maintain a relatively clear vortex shape, and the attenuation amplitude of the high-vorticity region is gentler. As the incoming flow velocity V_∞ increases, the resultant velocity V_S of the flapping wing increases, that is, the relative velocity increases, and the vorticity intensity of the flapping wing increases. However, a high incoming flow velocity means a fast convection velocity, which accelerates the detachment frequency of the vortices around the flapping wing cross-section and reduces the interaction between the leading-edge vortex and the wing surface; the angle of attack φ of the wing surface decreases, the vortices formed during the flapping process move more significantly toward the trailing edge of the flapping wing and detach near the trailing edge, the vorticity at the trailing edge of the flapping wing increases, and the pressure decreases, resulting in an increase in the drag on the flapping wing. This conclusion is consistent with that in Table 4.

Table 4. Lift impulse and thrust impulse of the flapping wing under different incoming flow velocities (f = 5 hz)

Incoming Flow Velocity		Net Lift Impulse ($N \times s$)	Net Thrust Impulse ($N \times s$)
V_∞ = 1 m/s	Before Optimization	0.0795	0.0059
	After Optimization	0.1596	0.0278
V_∞ = 3 m/s	Before Optimization	0.0961	0.0046
	After Optimization	0.2078	0.0204
V_∞ = 5 m/s	Before Optimization	0.0916	0.0034
	After Optimization	0.2318	0.0144

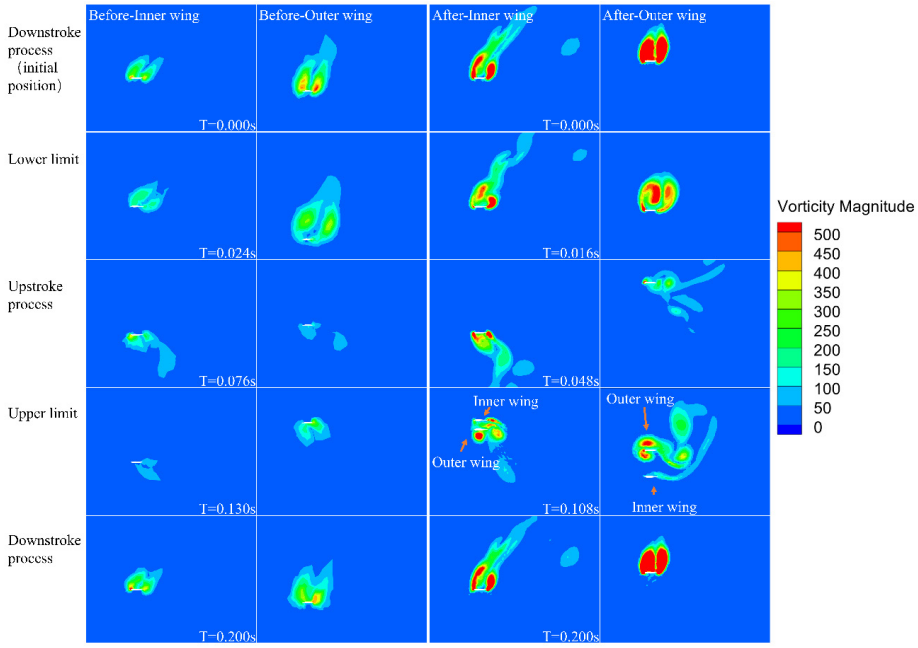

Figure 14. Vorticity distribution diagrams of the flapping wing cross-sections at different stages before and after optimization (f = 5 hz, V_∞ = 3 m/s)

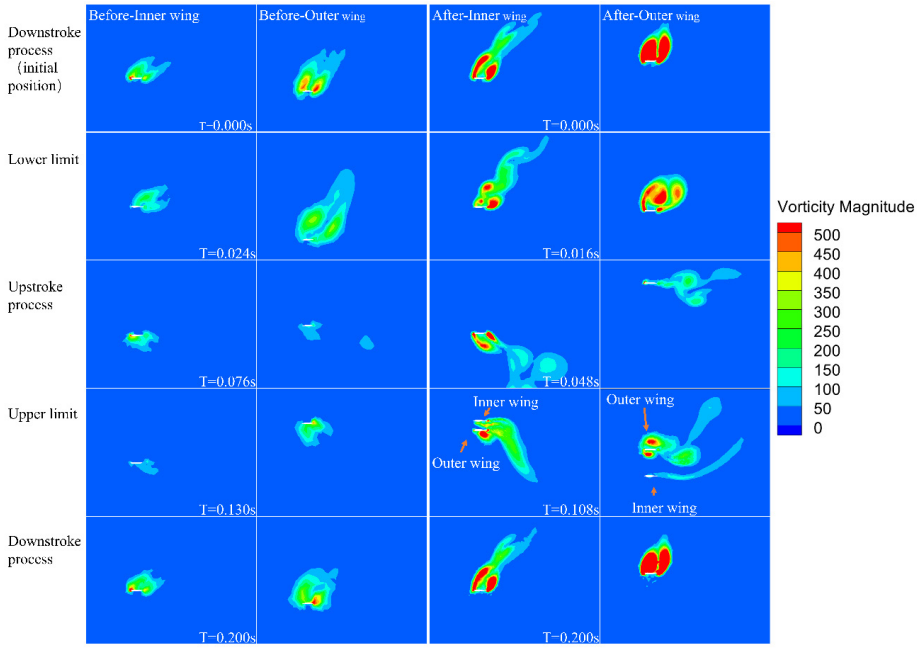

Figure 15. Vorticity distribution diagrams of the flapping wing cross-sections at different stages before and after optimization (f = 5 hz, V_∞ = 5 m/s)

4.3. Effect of flapping frequency on the aerodynamic characteristics of the flapping wing

The flapping frequency f is one of the important factors affecting the flight of flapping wing aircraft. Under the working condition with an incoming flow velocity of 1m/s, the flapping frequencies of the flapping wing are set to 2 Hz, 4 Hz, and 5 Hz in sequence. Figure 16 shows the effect of flapping frequency on the lift and thrust of the flapping wing. Since the time of one cycle of flapping wing motion varies under different flapping frequencies, for the convenience of comparison, the cycle is used as the abscissa in Figure 16. Table 5 shows the lift impulse and net thrust impulse of the flapping wing structure under different working conditions.

It can be seen from Figure 16 and Table 5 that under a certain incoming flow velocity, as the flapping frequency

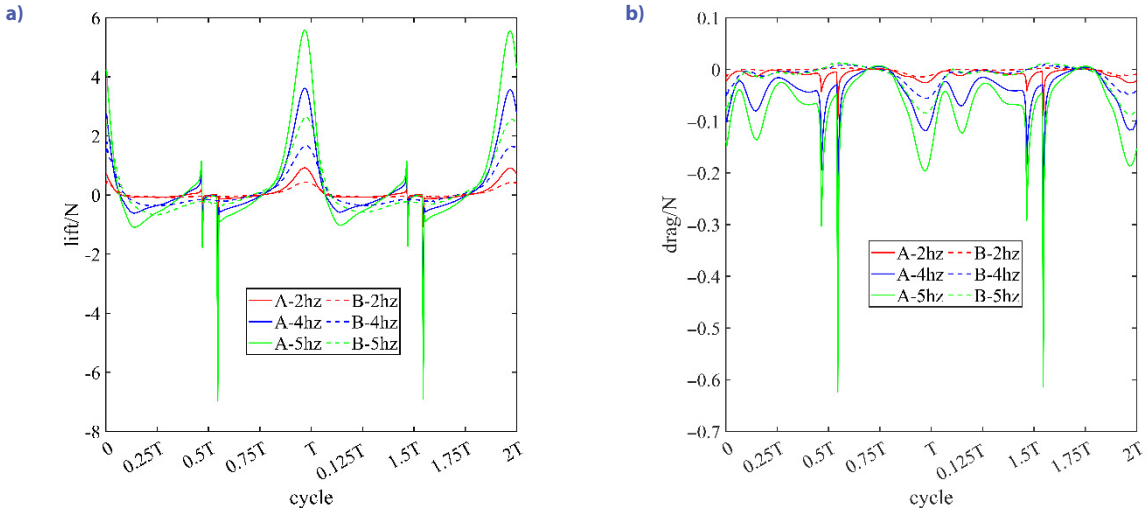

Figure 16. Lift curve and drag curve of the flapping wing under different flapping frequencies (V_∞ = 1 m/s): (a) – lift curve; (b) – drag curve

Table 5. Lift impulse and thrust impulse of the flapping wing under different flapping frequencies (V_∞ = 1 m/s)

Type		Net Lift Impulse ($N \times s$)	Net Thrust Impulse ($N \times s$)
f = 2 hz	Before Optimization	0.0379	0.0018
	After Optimization	0.0788	0.0086
f = 4 hz	Before Optimization	0.0660	0.0047
	After Optimization	0.1347	0.0211
f = 5 hz	Before Optimization	0.0795	0.0059
	After Optimization	0.1596	0.0278

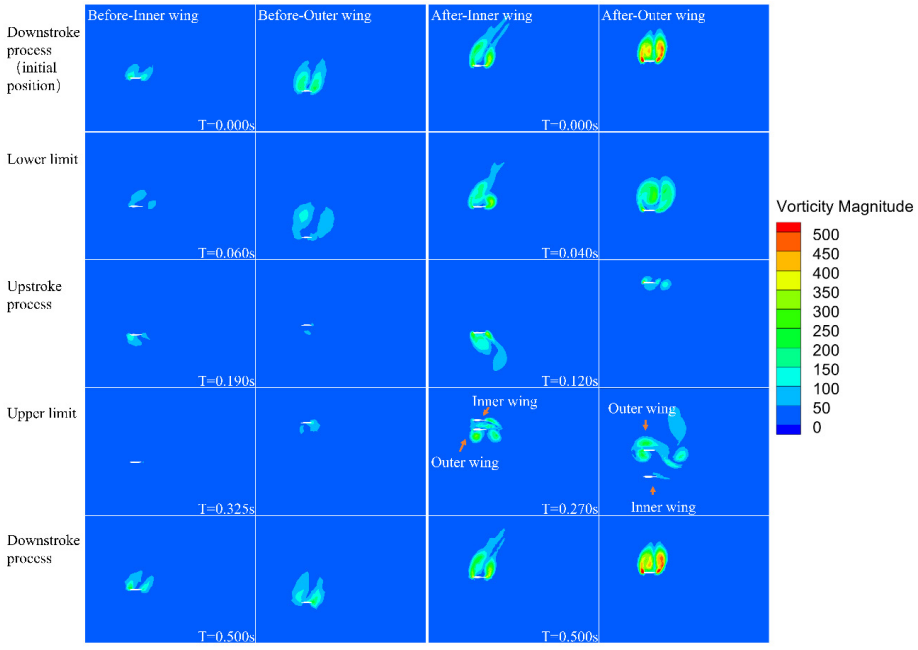

Figure 17. Vorticity distribution diagrams of the flapping wing cross-sections at different stages before and after optimization (f = 2 hz, V_∞ = 1 m/s)

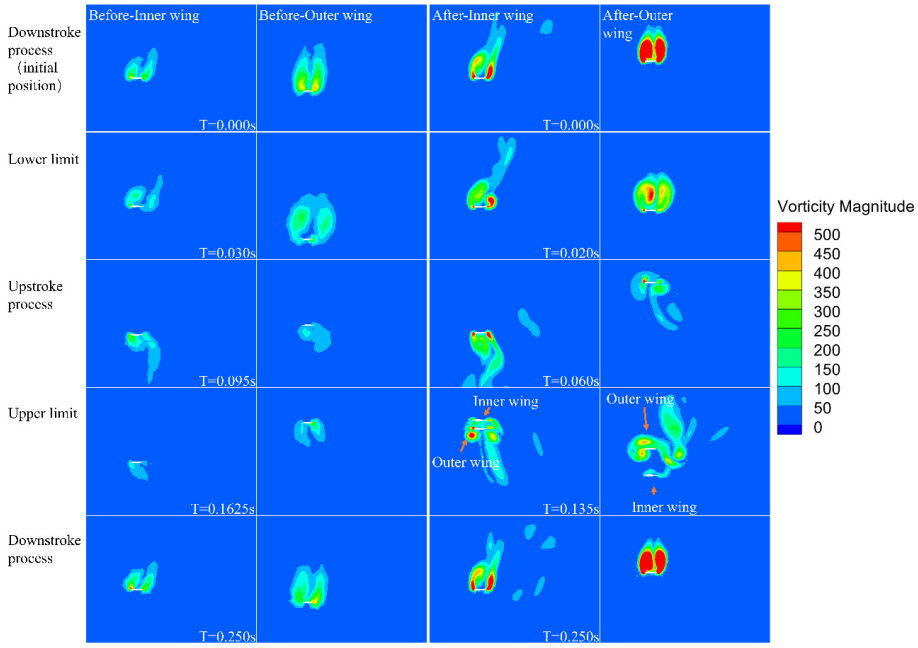

Figure 18. Vorticity distribution diagrams of the flapping wing cross-sections at different stages before and after optimization (f = 4 hz, V_∞ = 1 m/s)

increases, the net lift and net thrust on the flapping wing both increase, and as the flapping frequency increases, the growth rate of the aerodynamic force of the optimized flapping wing is much higher than that before optimization.

Figure 17 and Figure 18 show the vorticity distribution diagrams of the flapping wing cross-sections before and after optimization under the flapping frequency conditions of 2 Hz and 4 Hz, respectively.

It can be seen from Figures 12, 17, and 18 that under the same incoming flow velocity V_∞ and different flapping frequencies, the aerodynamic performance of the optimized flapping wing structure is still better than that of the flapping wing mechanism before optimization. The peak vorticity is increased by 12.5%, 11.8%, and 12% respectively, and the area of the high-vorticity region is increased by 26.7%, 31.3%, and 35% respectively. The flapping cycle of the flapping wing with a low frequency is long, and the airflow has sufficient time to return to a stable state. It is difficult for the wing surface to continuously roll up high-intensity vortices, and the high-vorticity region in the vorticity diagram decays and disperses quickly, resulting in low lift level and poor stability. As the frequency increases, the flapping cycle of the flapping wing becomes shorter, and the airflow separates frequently on the wing surface, which can quickly roll up high-intensity and well-concentrated vortex structures, providing continuous and efficient momentum contribution to the lift. The lift peak and average level reach the optimal state. In addition, regardless of the frequency, the optimized flapping wing structure has better vortex generation efficiency and intensity near the wing surface, and the lift peak and average value are improved.

5. Conclusions

This study investigates the geometric parameter optimization of a double-crank double-rocker two-segment flapping wing mechanism with the objective of lift maximization. By integrating kinematic modeling, genetic algorithm-based optimization, and unsteady aerodynamic simulations, the regulatory mechanism of geometric parameters on flapping wing motion characteristics and aerodynamic performance is clarified.

Geometric parameter optimization greatly improves the flapping kinematics of the wing. The main conclusions are summarized as follows:

1. After optimization, the swing range of the inner wing expands from about 57° to 90°. During the upstroke, the inner and outer wings fold faster with a smaller included angle, which effectively reduces aerodynamic resistance. In the downstroke, a higher wing deployment rate facilitates lift generation. Both wings gain larger rotational angular velocities, enabling stronger momentum exchange with ambient airflow. Overall, the optimized flapping wing achieves much better aerodynamic lift and thrust performance.
2. At a flapping frequency of 5 Hz and an incoming flow velocity of 1 m/s, lift impulse and thrust impulse rise by 100.75% and 371.2%, respectively. Across different flow velocities and flapping frequencies, the optimized configuration delivers higher net lift and net thrust with larger growth rates than the original design, verifying the validity of geometric parameter optimization. This study also reveals how incoming flow velocity and flapping frequency affect aerodynamic performance.

3. With a fixed flapping frequency, higher incoming flow velocity increases resultant velocity and vortex convection speed, producing greater lift as well as drag. With a fixed incoming flow velocity, a higher flapping frequency accelerates vortex formation and sustains high-strength vortex structures, thus improving lift and thrust. The optimized wing shows better stability and concentration of vortices, proving that optimized geometric parameters strengthen flow field control.
4. In terms of vorticity evolution, the optimized wing maintains compact, long-duration leading-edge vortices with low vorticity dissipation throughout the flapping cycle. By contrast, vortices of the original configuration disperse and decay rapidly, especially under high incoming flow. The results demonstrate that geometric optimization suppresses flow separation and cuts down aerodynamic energy loss.

Despite the promising results, several limitations of the present study should be acknowledged. Firstly, the aerodynamic analysis is conducted using rigid-wing numerical simulations, and the effects of wing flexibility, material properties, and mechanical clearances in the transmission system are not considered. These factors may influence the actual aerodynamic performance and structural durability of a real flapping wing system. Secondly, the optimization framework focuses on lift maximization as a single objective. The increased flapping amplitude and angular velocity after optimization may result in higher motor loads, increased energy consumption, and reduced fatigue life, which are important considerations for practical applications. Thirdly, although the numerical simulation setup is sufficient for comparative analysis, experimental validation through wind tunnel testing or prototype measurements has not yet been conducted.

Future work will focus on multi-objective optimization incorporating lift, energy efficiency, and structural reliability, as well as the inclusion of wing flexibility and aeroelastic effects. In addition, experimental validation using physical prototypes and wind tunnel tests, will be carried out to further verify the accuracy and applicability of the proposed optimization framework under realistic operating conditions.

Funding

This work was supported by the National Natural Science Foundation of China under Grant [number 52005106]; Guangdong University information technology key field under Grant [number 2021ZDZX1057].

Author contributions

JL and JZ conceived the study and proposed the research idea. HY conducted the numerical simulation and drafted the corresponding sections of the manuscript. XL performed the formula derivation and wrote the related sections. YL and ZH conducted the literature review and drafted the introduction section. ZW revised and polished the entire manuscript.

Disclosure statement

The author(s) declared no potential conflicts of interest with respect to the research, authorship, and/or publication of this article.

References

Addo-Akoto, R., Han, J. S., & Han, J. H. (2021). Roles of wing flexibility and kinematics in flapping wing aerodynamics. *Journal of Fluids and Structures*, *104*, Article 103317. https://doi.org/10.1016/j.jfluidstructs.2021.103317

Ansari, S. A., Knowles, K., & Zbikowski, R. (2008). Insectlike flapping wings in the hover part I: Effect of wing kinematics. *Journal of Aircraft*, *45*(6), 1945–1954. https://doi.org/10.2514/1.35311

Bhat, S. S., Zhao, J. S., Sheridan, J., Hourigan, K., & Thompson, M. C. (2020). Effects of flapping-motion profiles on insect-wing aerodynamics. *Journal of Fluid Mechanics*, *884*, A8.1-A8.23. https://doi.org/10.1017/jfm.2019.929

Choi, J., & Park, G. (2017). Multidisciplinary design optimization of the flapping wing system for forward flight. *International Journal of Micro Air Vehicles*, *9*(2), 93–110. https://doi.org/10.1177/1756829317691990

Dong, Y., Song, B., Yang, W., & Xue, D. (2023). Optimization of a twistable hovering flapping wing inspired by giant hummingbirds using the unsteady blade element theory. *Applied Sciences*, *13*(9), Article 5704. https://doi.org/10.3390/app13095704

Gehrke, A., & Mulleners, K. (2020). Phenomenology and scaling of optimal flapping wing kinematics. *Bioinspiration & Biomimetic*, *16*(2), Article 026016. https://doi.org/10.1088/1748-3190/abd012

Huang, M. (2019). Optimization of flapping wing mechanism of bionic eagle. *Proceedings of the Institution of Mechanical Engineer, Part G: Journal of Aerospace Engineering*, *233*(9), 3260–3272. https://doi.org/10.1177/0954410018794339

Liu, C., Li, P., Song, F., Stamhuis, E. J., & Sun, J. (2022). Design optimization and wind tunnel investigation of a flapping system based on the flapping wing trajectories of a beetle's hindwings. *Computers in Biology and Medicine*, *140*, Article 105085. https://doi.org/10.1016/j.compbiomed.2021.105085

Lang, X. Y., Song, B. F., Yang, W. Q., & Song, W. (2021). Aerodynamic performance of owl-like airfoil undergoing bio-inspired flapping kinematics. *Chinese Journal of Aeronautics*, *34*(5), 239–252. https://doi.org/10.1016/j.cja.2020.10.017

Ling, Y., Liu, B., Zhang, H., Bo, L., & Liu, M. (2025). Analysis and optimization of flapping-wing mechanism based on genetic algorithm. *Machines*, *13*(3), Article 197. https://doi.org/10.3390/machines13030197

Li, P., Ai, Z., & Zhang, M. (2025). Optimized actuator design for flapping-wing robots: A multi-objective approach to mimic natural flapping dynamics. *Advances in Mechanical Engineering*, *17*(4), 1–12. https://doi.org/10.1177/16878132251335551

Rakotomamonjy, T., Ouladsine, M., & Moing, T. L. (2007). Modelization and kinematics optimization for a flapping-wing microair vehicle. *Journal of Aircraft*, *44*(1), 217–231. https://doi.org/10.2514/1.22960

Wang, Z. L., Hu, X. R., & Wu, Y. D. (2019). Energy-efficient wing design for flapping wing micro aerial vehicles. *Journal of Mechanical Science and Technology*, *33*(9), 4093–4104. https://doi.org/10.1007/s12206-019-0804-1

Xu, Q. Y., Zhu, J. Y., Zhu, M. K., & Xie, P. (2024). Optimization of kinematic parameters of 3D forward flapping wing. *Journal of Aerospace Power*, *39*(9), Article 20220083. http://www.jasp.com.cn/hkdlxb/en/article/doi/10.13224/j.cnki.jasp.20220083

Zhou, L., Zhang, Z. H., Wang, J. H., Zhao, Q. L., & He, G. P. (2022). Research status and development of flapping wing aircraft. *Journal of Ordnance Equipment Engineering*, *43*(8), 44–54. https://doi.org/10.11809/bqzbgcxb2022.08.007

Zhang, Y. X., Wang, X. J., Wang, S. P., Huang, W., & Weng, Q. (2021). Kinematic and aerodynamic investigation of the butterfly in forward free flight for the butterfly-inspired flapping wing air vehicle. *Applied Sciences*, *11*(6), Article 2620. https://doi.org/10.3390/app11062620

Zheng, H. Y., Xie, F. F., Ji, T. W., & Zheng, Y. (2020). Kinematic parameter optimization of a flapping ellipsoid wing based on the data informed self-adaptive quasi-steady model. *Physics of Fluids*, *32*(4), 77–105. https://doi.org/10.1063/1.5144642

Zhang, H., Wen, C., & Yang, A. (2016). Optimization of lift force for a bio-inspired flapping wing model in hovering flight. *International Journal of Micro Air Vehicles*, *8*(2), 92–108. https://doi.org/10.1177/1756829316653698